

Article

Identification of Roof Surfaces from LiDAR Cloud Points by GIS Tools: A Case Study of Lučenec, Slovakia

Marcela Bindzarova Gergelova ^{1,*} , Slavomir Labant ¹ , Stefan Kuzevic ² ,
Zofia Kuzevicova ¹  and Henrieta Pavolova ²

¹ Institute of Geodesy, Cartography and Geographical Information Systems, Faculty of Mining, Ecology, Process Control and Geotechnology, Technical University of Kosice, Letna 9, 042 00 Kosice, Slovakia; slavomir.labant@tuke.sk (S.L.); zofia.kuzevicova@tuke.sk (Z.K.)

² Institute of Earth Resources Ecology, Faculty of Mining, Ecology, Process Control and Geotechnology, Technical University of Kosice, Letna 9, 042 00 Kosice, Slovakia; stefan.kuzevic@tuke.sk (S.K.); henrieta.pavolova@tuke.sk (H.P.)

* Correspondence: marcela.bindzarova.gergelova@tuke.sk; Tel.: +421-55-602-2916

Received: 21 July 2020; Accepted: 18 August 2020; Published: 23 August 2020



Abstract: The identification of roof surfaces is characterized by a sequence of several processing steps. The boundary detection of different types of roof is realized from light detection and ranging (LiDAR) cloud points and can confirm the real boundary of the roof. In the process of processing LiDAR data, shortcomings have been found regarding the inappropriate classification of points (class 6 “buildings”) concerning the roofs (the points of the building facade were marked as outliers and reclassified). In cases of insufficient point density, there is a problem with not being able to capture either the roof boundary or small roof objects, along with the possible occurrence of gaps inside the roof areas. This study proposes a processing procedure in a geographic information system (GIS) environment that advocates the identification of roof surfaces based on the LiDAR point cloud. We created the contours of a roof surface boundary with a simplified regular shape. From 824 roofs in the studied area, six different types of roof were selected, which this study presents in detail. The expected result of the study is the generation of segments inside the roof boundary. The study also includes the visualization of the outcomes of the spatial analyses of the identified roof surfaces, which forms the basis for determining the potential of solar systems with respect to green roofs for the development of smart city buildings.

Keywords: buildings; roofs; LiDAR; point cloud; segmentation; feature extraction; GIS

1. Introduction

Today, more than two thirds of the union’s population live in cities, consuming around 80% of its energy and producing up to 85% of Europe’s gross domestic product [1]. Cities are thus becoming the birthplace of challenges, such as environmental pollution, social inequalities, and traffic restrictions, which cause persistent social, economic, or environmental problems. These impacts cause effects on spatial changes in the way land is used and transformed in favor of development [2,3]. Spatial and functional changes related to classes of urban areas characterize the information contained in the Corine Land Cover (CLC) classification database [4,5].

Within the construction of intelligent cities and their sustainability, one challenge is the creation of three-dimensional (3D) models of object buildings. The 3D city model is an essential part of several different applications and analyses related to infrastructure [6,7], planning and urbanism [8,9], solar radiation modeling in urban areas [10,11], and the potential for building green roofs in cities [12,13],

etc. These location models are often not available, are of low image quality, or the data is out of date. Experts are looking for a solution at the local level, intending to maximally support and develop the idea of a sustainable city through the Ministry of Investment, Regional Development, and Informatization of the Slovak Republic (www.smartcity.gov.sk) and the Slovak Smart City Cluster (smartcluster.sk). Both the population and the results of its activities are increasingly beginning to pose a threat to society. Increasing demands on consumption (a consumerist way of life) bring with them a whole group of various social problems, the common denominator of which is the preservation of the sustainability of urban space [14,15].

An important part of the city's information systems is its data on buildings, which require frequent updating. For this reason, the detection of buildings and the changes in buildings play an important role. Data obtained by aerial contactless collection methods (light detection and ranging (LiDAR), Remote Sensing) are now available to the public for further processing. The problem of object detection in satellite/aerial images has been addressed in recent years by several research papers. Aerial photogrammetry [16], high resolution aerial satellite images [17], interferometric synthetic aperture radar (InSAR) [18], and the LiDAR point cloud [19,20] can be used as inputs for object detection. The study by Awrangjeb et al. [21], which combines input data from the LiDAR system and multispectral imagery, and other works [22,23] recommend a combination of input data for more accurate object capturing.

The detection of buildings in urban areas itself involves solving several problems related to objects located near buildings, such as trees and power lines. Similarly, problems can occur with the different surface materials of buildings, which may have different reflective properties. The Snake model is often used to detect buildings from high-resolution aerial imagery for use in urban environments [24,25]. Both studies confirm the suitability of using this model in the case of urban development with complex structures. The paper [26] combines the Snake model with the watershed segmentation technique.

Segmentation is a technique used to divide a surface into several non-overlapping parts. Watershed segmentation is a robust method based on mathematical morphology [27]. In the field of the watershed segmentation procedure, several improved algorithms have been designed and developed in recent years [28,29], as well as the possibility of combining these with the deep learning method [30] to improve image segmentation.

Traditional methods of data collection using photogrammetry for the creation of 3D models of objects have been replaced in recent years by LiDAR aerial laser scanning and the use of special processing techniques and procedures [20]. The basis of LiDAR data processing is an unclassified point cloud. In order to extract classes of buildings from this cloud, it is necessary to filter the data using classification methods and techniques such as the support vector machine (SVM) [31], methods using local neighborhood statistics [32], and methods based on neural networks [33] with improvements [34].

Segmentation-based filtering group points are first based on the local neighborhood property. The segments are then classified into ground and non-ground. An overview of the algorithms for ground data classification can be found in [35]. Data classified as non-ground were further divided into several classes (6—buildings; 9—water, etc.). The properties of a point describe its characteristics and its surroundings, but, due to interfering phenomena and observation errors, incorrect data classification can occur [36].

The extraction of building/roof boundaries is of great importance in the creation of smart city building. The introduction of the automation process into the field of object detection/segmentation/extraction [37–39] is an important part of the 3D object modeling system regarding buildings [40]. A paper by Zhang et al. [41] focuses on roof extraction using the spectral clustering of straight-line segments, in which the authors point to the efficiency of extracting large roof areas. For extracting shapes in two-dimensional (2D) space, Santos et al. [42] use the alpha-shape algorithm, which shows resistance to density changes in LiDAR data.

The main aim of this scientific study is the segmentation and extraction of roof objects in residential areas in the geographic information system (GIS) environment. The methodology used allows the

segmentation and extraction of roof objects over a larger area and can perform analyses of geometric and topological parameters. We chose the LiDAR point cloud, photogrammetric images, and vector data from information systems in Slovakia as input data. The LiDAR data used in this study supplied already classified by the supplier (the Geodesy, Cartography, and Cadastre Authority of the Slovak Republic, GCCA SR). According to the Awrangjeb methodology [38], the generation of roof contours is performed on filtered LiDAR data (class 6—buildings). An irregular roof contour was created, which was then generalized to a regular roof contour. For a more detailed characterization of the roof area, the modeling of the ridge based on the methodology of watershed segmentation presented in the work of Merabet et al. [43].

Part of the solution also focusing on errors that may occur in the input data and their processing. The application of the chosen methodology is possible not only in a small area but also at the level of city districts or entire cities. The main benefits of this study are: a critical view of the errors in the input data; the analysis of the raster cell size entering the processing; the design of the extraction procedure of roof objects for processing in the GIS environment; automation to create a detailed roof model; the visualization of analyses of selected geometric and topological parameters of roof surfaces, with the possible application in the field of potential determination for solar systems and green roofs.

2. Materials and Methods

This part of the study presents the study area, data sources, and methodology for identifying roof objects concerning their selected geometric and topological parameters. The starting point of the processing works is a workflow diagram characterizing the segmentation of the roof surfaces (Figure 1).

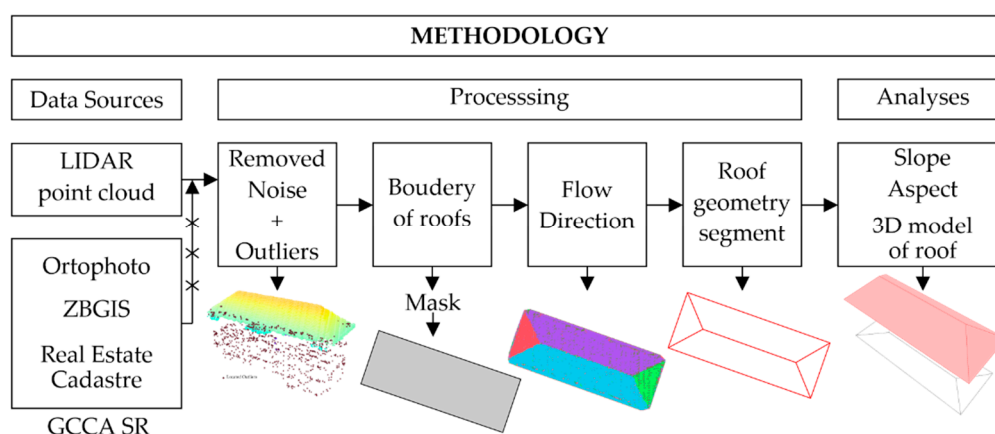


Figure 1. The workflow of the roof extraction.

2.1. Study Area

The territory of the district town of Lučenec, which lies in the central part of the Lučenec basin (Figure 2) at an altitude of 194 m above sea level, was chosen for the solution. With its population of 27,739 (status of the permanent population as of 31 December 2019, the Statistical Office of the Slovak Republic), it is in 22nd place out of 141 cities in Slovakia. The city is located in a warm climatic region, being also a dry subregion with a cold winter. The average annual air temperature is 9.1 °C. The mean annual sums of global radiation reach values around 1250 kWh.m⁻². The annual sums of sunshine range from 1800 to 1900 h [44].

For the case study, an area with dimensions of 1.5 km × 1.15 km = 1.725 km² was chosen (Figure 2b). The study area's choice took into account the availability of data, especially the ongoing process of aerial laser scanning (ALS) of the entire territory of Slovakia (www.geoportal.sk/sk/udaje/lis-dmr/). ALS takes place from the western part to the east, with the expected completion in 2023. The choice of the area also influenced by the representation of all types of roof areas of the buildings (Figure 3: industrial buildings, residential houses, and family houses).

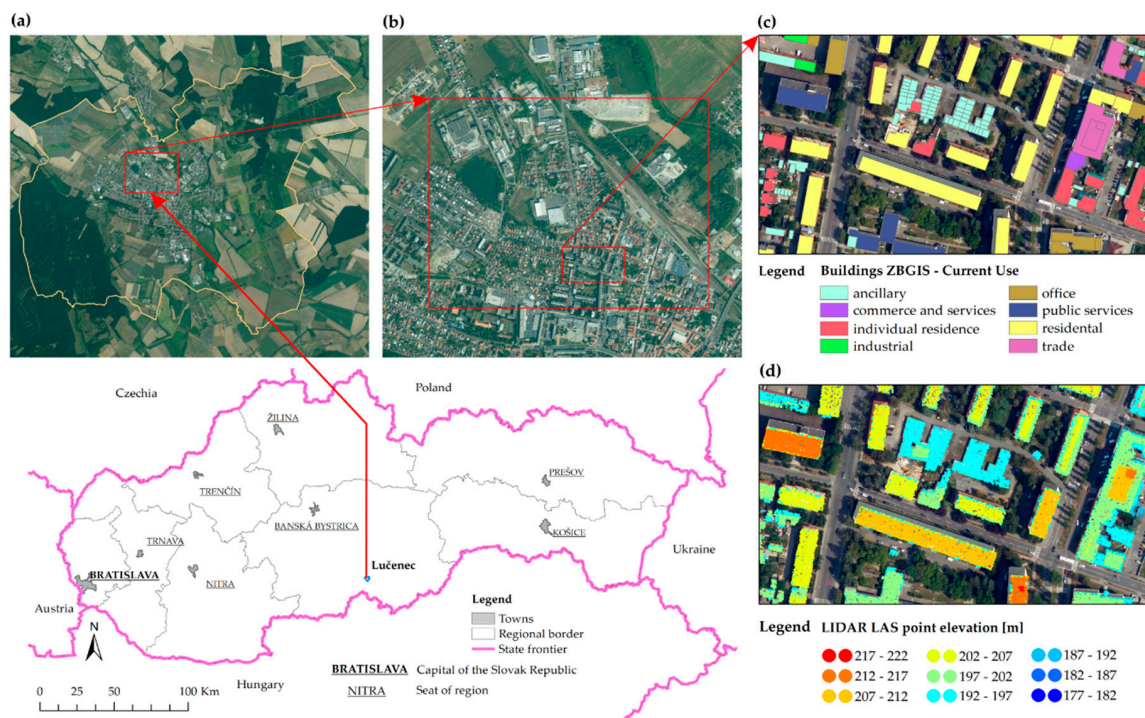


Figure 2. Location of the study area of the Slovak Republic. (a) Lučenec district on the orthophoto mosaic; (b) study area—part of the town Lučenec; (c) ZBGIS data; (d) LiDAR point cloud-class of buildings.



Figure 3. Overview of the representation of roof areas of the buildings in the study area: (a) industrial building; (b) apartment buildings; (c) family houses.

2.2. Data Sources

Data from aerial laser scanning (*.las) and aerial photogrammetry (*.tiff) was used as input data. Data from the Basic Database for the GIS (ZBGIS) were available to display the building footprints. All the source data were provided by the GCCA SR. The buildings.shp file contained data for 2514 objects. This data then processed via GIS (the combination of ArcMap 10.7.1 and ArcGIS Pro 2.4.3). An overview of the basic characteristics of the input data is shown in Table 1.

The point cloud of the area of interest obtained from the ALS (LiDAR) contained 33,019,202 points stored in 6 files with the extension *.las. The average point spacing of the study area is 0.23 m. The average point cloud density in our study was 19 points/m². Redweik et al. [45] also worked with approximately the same density of 20 points/m². In the study [46], they worked with LiDAR data with an average density of 6.75 points/m² and in research [47] with an average density of 0.44 point/m². A study by Triglav Čekada et al. [48] is the recommended point density for a built-up area with vegetation of 12 to 20 point/m².

Table 1. Input data for roof modeling.

Dataset	Release Date	Format	Characteristic
Orthophoto mosaic ¹ (Central part of the Slovakia)	2018	*.tiff *.tfw	Resolution: 25 cm/pixel Number of channels: 3 (RGB, 8-bit) Coordinate system: D-UTCN (UTCN), code EPSG: 5514 Accuracy: RMSE _{xy} = 0.30 m CE ₉₀ = 1.5175 × RMSE _{xy} = 0.45 m CE ₉₅ = 1.7308 × RMSE _{xy} = 0.52 m
LiDAR ¹ point cloud	XI. 2018 –IV. 2019	*.las	An altitude accuracy of cloud points: 0.03 m A position accuracy of cloud points: 0.11 m The average density of points (last reflection): 19 pt/m ² Coordinate system: D-UTCN (UTCN03)
Buildings ZBGIS ¹	2005–2018	*.shp	Attribute table FACC (DIGEST code) Objects update date = 2005–2018 horizontal and vertical accuracy code: 1 = Geodetic (<0.1 m) 2 = Photogrammetric (<1 m) 3 = Photogrammetric (<5 m) 4 = Photogrammetric on relief (<1 m) 997 = Estimated height (>5 m) Coordinate system: D-UTCN (UTCN), EPSG code: 5514
Buildings–Real Estate Cadastre ¹	VI.2020	*.shp *.vgi	The set of geodetic information Vector cadastral map Coordinate system: D-UTCN (UTCN), EPSG code: 5513

¹ Geodesy, Cartography, and Cadastre Authority of the Slovak Republic.

The provider already classified the LiDAR point cloud into nine classes for the study. Classes 2—ground and 6—buildings were necessary for our case study. An essential step in the processing was to check and possibly remove erroneous data from the *.las file, which could bring uncertainties to the expected result (presence of outliers).

2.3. Transformation of Coordinate Systems

The input data used are in different coordinate systems depending on their national implementations. To ensure quality results, the data are first transformed into a single binding coordinate system. Geodetic reference systems generally consist of a datum and a coordinate system (Figure 4). The datum defines the origin position, scale, and orientation of the coordinate system axes, and the coordinate system is the assignment of coordinates to points.

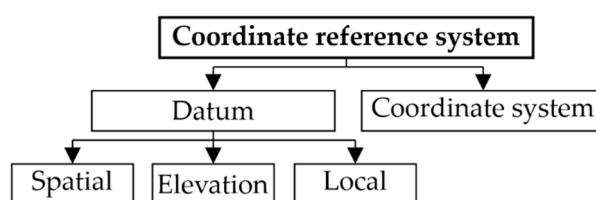


Figure 4. Scheme of the definition of geodetic reference systems.

Binding the geodetic reference systems and their valid implementations on the territory of Slovakia (Table 2) is determined by Decree 300/2009 Coll. Geodesy, Cartography, and Cadastre Authority of the Slovak Republic (<https://www.slov-lex.sk/pravne-predpisy/SK/ZZ/2009/300/20140215>). This decree implements the Act of the National Council of the Slovak Republic no. 215/1995 Coll. on geodesy and cartography. The implementation of a geodetic reference system involves the determination of coordinates, heights, or gravity accelerations related to physical points stabilized on the earth's surface.

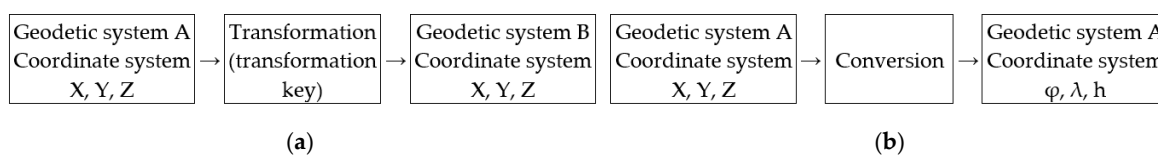
Table 2. Binding geodetic reference systems and their implementation for the needs of solving the case study (<https://www.geoportal.sk/sk/geodeticke-zaklady/geodeticke-systemy-transformacie/>).

Geodetic Reference System	Code	Implementation of the Geodetic Reference System	Code	EPSG Code
European Terrestrial Reference System 1989	ETRS89	Slovak Terrestrial Reference Framework 2009	SKTRF09 = ETRF2000	4937 (3D- φ, λ, h) 4258 (2D- φ, λ) 4936 (3D-X, Y, Z)
Datum of Unified Trigonometric Cadastral Network	D-UTCN	Uniform Trigonometric Cadastral Network	UTCN	2065 (Ferro) 5513 (Greenwich)
		Uniform Trigonometric Cadastral Network 2003	UTCN03	8352 (Greenwich)
Baltic Vertical Datum -After Adjustment	BVDaA	Baltic Vertical Datum -After Adjustment	BVDaA (1957)	8357

ETRS89 is identical to the International Terrestrial Reference System (ITRS) in the 1989.0 eras and is fixed on a stable part of the Eurasian tectonic plate. The currently valid national implementation of ETRS89 is SKTRF09, which corresponds to ETRF2000, epoch 2008.5. SKTRF09 represents the spatial coordinates of all A and B points of the ŠPS class and their accuracy characteristics.

D-UTCN is defined by Bessel's ellipsoid 1841 and Křovák's representation as a rectangular planar coordinate system (x-axis points south and y-axis west). In the Slovak Republic, D-UTCN has two implementations. 1) UTCN is the original implementation and is binding for documenting and taking over the results of geodetic and cartographic activities for the information system of geodesy and cartography or real estate cadastre. 2) UTCN03 is a new implementation, determined using global navigation satellite systems (GNSS) observations and primarily intended for surveying works.

Transformation or conversion can be used to convert between geodetic coordinate systems (Figure 5). The transformation parameters can only be derived empirically using identical points that have specified coordinates in both systems. In general, the conversion is unambiguous and with a high accuracy. A global transformation key (GTK) is used to transform point coordinates between ETRS89 (ETRF2000) and D-UTCN (UTCN03). GTK represents seven transformation parameters calculated by the spatial similarity transformation by the Burša–Wolf model. The GTK parameters are given in Table 3, according to [49].

**Figure 5.** Explanatory diagram for (a) the transformation of the (b) converting.**Table 3.** The transformation parameters between ETRS89 and D-UTCN.

The Direction of the Transformation			
ETRS89 (ETRF2000) → D-UTCN (UTCN03)		D-UTCN (UTCN03) → ETRS89 (ETRF2000)	
The shift in the axis direction	Axis rotation	The shift in the axis direction	Axis rotation
$T_X = -485.014055$ m	$R_X = 7.78625453''$	$T_X = 485.021$ m	$R_X = -7.786342''$
$T_Y = -169.473618$ m	$R_Y = 4.39770887''$	$T_Y = 169.465$ m	$R_Y = -4.397554''$
$T_Z = -483.842943$ m	$R_Z = 4.10248899''$	$T_Z = 483.839$ m	$R_Z = -4.102655''$

Parameter of the scale changes: $m = 0.000000$ ppm.

2.4. Detection, Segmentation, and Extraction of Roof Objects

Knowledge of the geometry/typology of roofs is essential for various spatial analyses based on this group of objects. The process of detecting roof planes, ridges, hips, and valleys uses the assumption that all roof surfaces form parts with different slopes and orientations [50]. Another assumption of this study is that only planar roof segments can be detected, extracted, and segmented in further processing. This approach used into account in the group of the following types of roofs monitored by us (Figure 6).

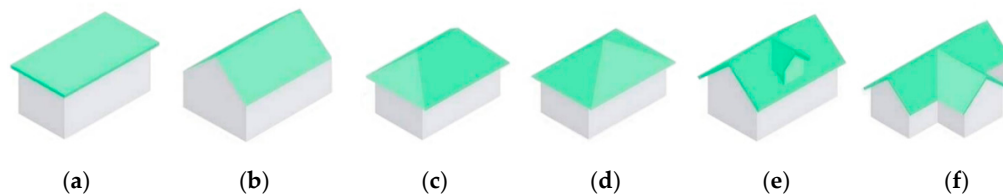


Figure 6. Selected basic types of roofs with the specified number of segments: (a) flat—1 segment; (b) open gable—2 segments; (c) hip—4 segments; (d) pyramid hip—4 segments; (e) dormer—4 segments; (f) cross-gabled—5 segments.

In the study, we applied GIS-based methods to the detection, extraction, and segmentation of building roofs. The choice of the solution of this part of the study was from professional work with a similar focus Palmer et al. [51], Höfle et al. [40], and Margolis et al. [52]. One of the aims of this study is to obtain a 2D/3D outline of a bounded polygon of the roof surface. In terms of methodological approaches, there are various recommendations from scientific studies on the issue applied in the study [43,53].

To represent the real shape of the roof ridge, the study uses a method derived from the modeling of river basins—namely, modeling the flow direction. Three types of flow direction methods—the deterministic eight-neighbors method (D8) [54], Multiple Flow Direction (MFD) [55], or D-Infinity (DINF) [56]—can be used in the GIS environment to capture the outflow direction. These methods make it possible to determine the characteristic regions for the flow direction, thus defining the boundaries of the individual roof segments. The process of extracting the selected group of objects follow a sequence of steps (Figure 1).

We used a point cloud of the classification codes for 6—buildings to extract the polygons of roof objects from the LiDAR base. All the recommendations for the conversion of the buildings raster into polygons were met by setting the following parameters:

- a minimum area of the roof segment;
- preserving the squareness of the edges of objects (90°);
- the boundary of the roof is made of a fully enclosed polygon without unnecessary holes (gaps).

3. Results and Discussion

3.1. Comparison of Dataset Integrity from Available National Spatial Databases

The real identification of the roof areas of residential buildings in this study was carried out based on the LiDAR data. The original intention of the study was to generate roof outlines based on the background data from available sources of map services (ZBGIS, Real Estate Cadastre). It is important to emphasize that the processing process itself was some to extent marked by the uncertainties identified. Uncertainties were associated with data processed and stored in different national implementations (UTCN-UTCN03). In the interval of updating objects, the data obtained were from different periods. The content of available datasets of ZBGIS map services is available in national implementations:

- Real Estate Cadastre—Buildings D-UTCN/UTCN;
- ZBGIS—Buildings D-UTCN/UTCN-UTCN03;

- Orthophoto mosaic D-UTCN/UTCN03.

The data used in this study are in both D-UTCN implementations (UTCN and UTCN03). Failure to differentiate these national implementations during processing leads to increased inaccuracies and may cause erroneous results. Figure 7 shows the contents of the ZBGIS and Real Estate Cadastre databases based on the orthophoto. By comparing these background data, outdated are visible either in Figure 7b or in Figure 7c. The shopping center presented in Figure 7 is absent from the ZBGIS database, while the Real Estate Cadastre database displays this object. Another problematic aspect is the content of the database registered in the Real Estate Cadastre—dataset “Zappar” (Figure 7c—dark blue line). This part of the database contains information on real estate, registered until 2001. So far, the data are not registered in the official dataset “Kladpar”—blue area.

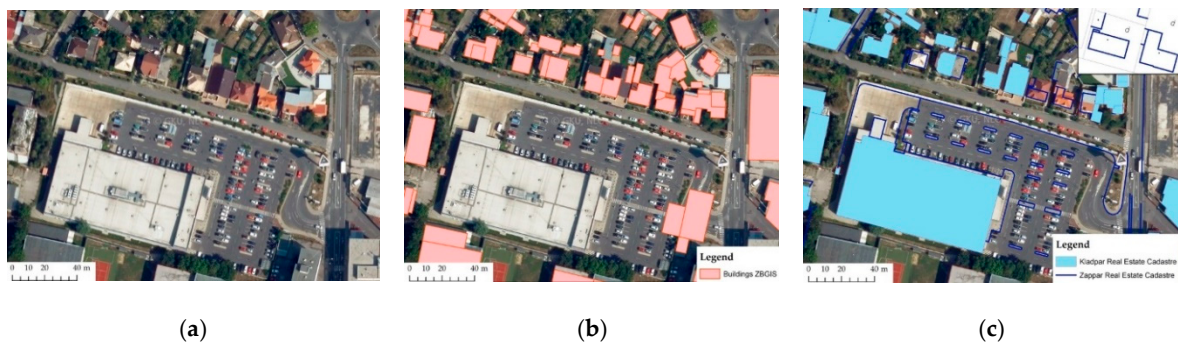


Figure 7. Graphical representation of available background data: (a) orthophoto of a part of the study area; (b) non-updated content of ZBGIS-Buildings pink field; (c) Real Estate Cadastre: “Kladpar”—blue field, “Zappar”—dark blue line (to the year 2001).

When comparing the compatibility of graphical background data, “point to point” shifts are evident. Figure 8a Buildings Real Estate Cadastre vs. Buildings ZBGIS UTCN shows the detected displacement of up to 1.5 m. Figure 8b Buildings Real Estate Cadastre vs. Buildings ZBGIS UTCN03 shows the detected displacement of up to 2.0 m. Figure 8c Buildings ZBGIS UTCN03 vs. Buildings ZBGIS UTCN shows the detected displacement of up to 0.6 m.

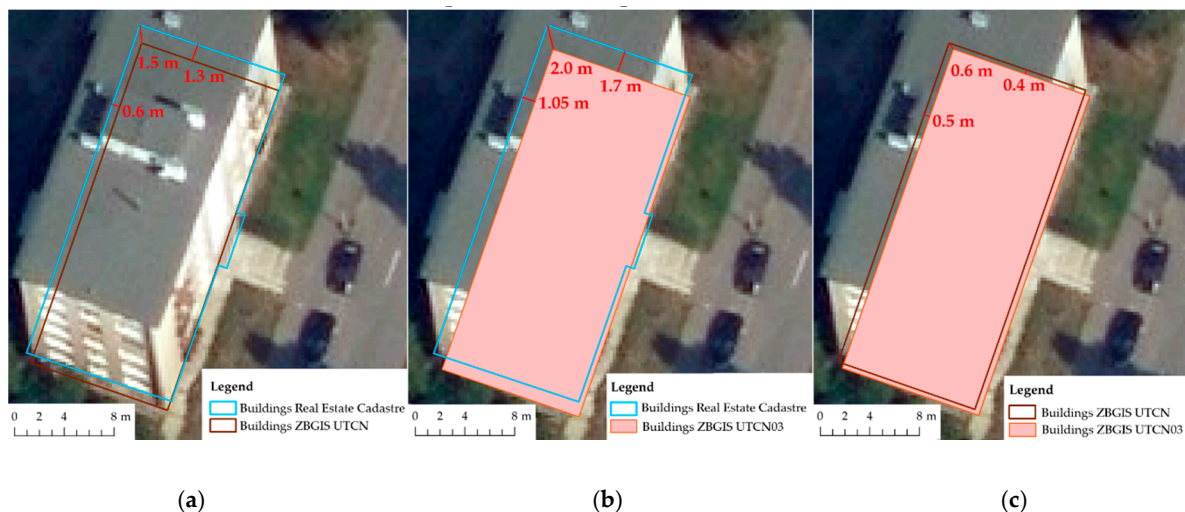


Figure 8. Graphical representation of the comparison (non-identity) of the background data: (a) Buildings Real Estate Cadastre (“Kladpar”—blue line) vs. Buildings ZBGIS UTCN; (b) Buildings Real Estate Cadastre (“Kladpar”—blue line) vs. Buildings ZBGIS UTCN03 (pink field); (c) Buildings ZBGIS UTCN03 (pink field) vs. Buildings ZBGIS UTCN (brown line).

3.2. Input Data Processing—LiDAR Point Cloud

Based on the confirmed inaccuracies (outdated, non-identity) of the underlying data (shown in Figures 7 and 8), only the LiDAR point cloud data were selected as the basis for calculation. Table 4 presents the quantitative characteristics of the classified point cloud of the subject area in the case study.

Table 4. Characteristics of LiDAR point cloud classification.

Classification	Absolute Frequency	Relative Frequency
Unassigned	1,194,562	3.62%
Ground	18,036,417	54.62%
Low vegetation	1,882,184	5.70%
Medium vegetation	1,240,739	3.76%
High vegetation	3,883,862	11.76%
Buildings	6,599,697	19.99%
Noise	3,888	0.01%
High noise	10,808	0.03%
Water	167,045	0.51%
Total number of points	33,019,202	100.00%

The buildings partially located in the selected location and outside have been removed from the point cloud. The number of points of incomplete objects was 289,735, which represented 4.4% of the total number of points in the building class. The initial processing of the LiDAR data is on the verification of the occurrence of an inappropriate set of points in the “noise” category, which could distort/inaccurate the results in further processing. The following Figure 9 presents a sample of classified LiDAR data containing unwanted points identified as “noise”. These bad points have moved to a separate “high noise” class. Subsequently, there was processing with a dataset of “cleaned” data according to the procedure (Figure 1).

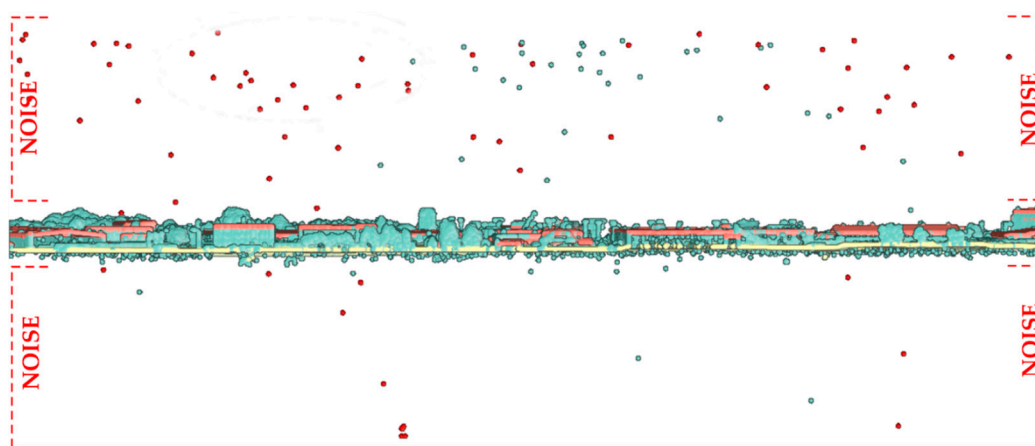


Figure 9. Cross-section of LiDAR point cloud with noise.

For further processing, classified (*.las) files were displayed in the form of a point cloud according to the required classes. Based on the orthophoto (Figure 10a), the result of displaying the point class “ground” (Figure 10b) and the point class “building” (Figure 10c) of the *.las dataset is presented.

In the process of the automatic classification of LiDAR data, in some cases the object is incorrectly identified. By comparing the orthophoto and the classified LiDAR data, incorrect classifications of objects can be found—e.g., a bus included in the “building” class (Figure 11a). There are also outdated issues related to the different schedules for the implementation of aerial scanning and aerial photogrammetry. By comparing these results, it is possible to find, e.g., LiDAR data that show a completed family house (Figure 11b) or a removed/demolished building (Figure 11c).

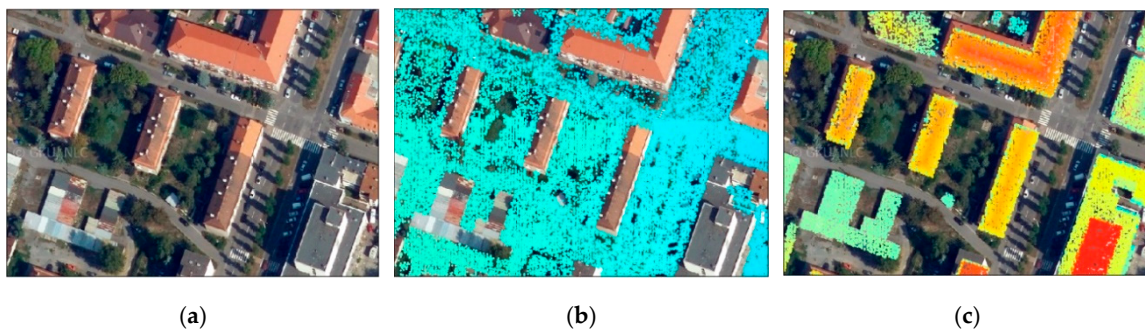


Figure 10. View of a representation of the selected cloud point class: (a) view of a selected area on the orthophoto; (b) view with ground points; (c) view with building points.

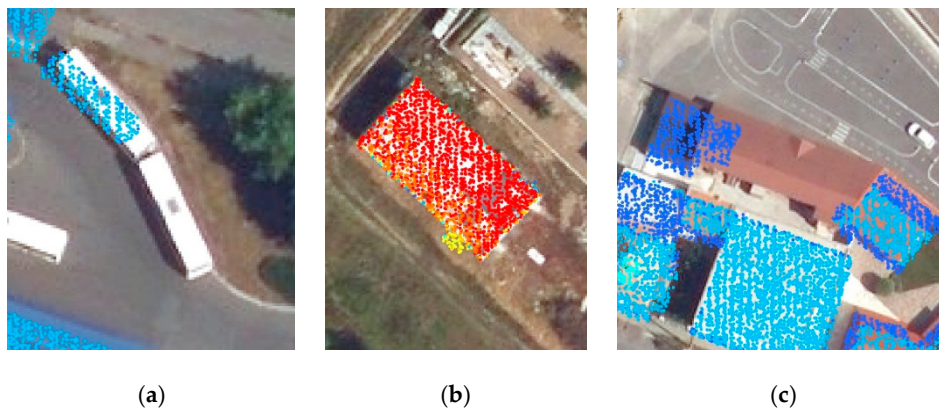


Figure 11. Comparison of the orthophoto map and classified LiDAR point cloud: (a) incorrect classification of the object-parked bus at the bus station; (b) outdated orthophoto map—the family house according to LiDAR that is built already; (c) topicality of LiDAR—the building according to the orthophoto map is still existing.

Before identifying the roof areas of buildings, it was necessary to remove the set of points that were on the facade of the buildings and possibly other outliers. The display of these remote points, which do not belong to the point cloud of the roof, should be presented in 3D space. The following Figure 12 shows the points belonging to the “building” class with the identified outliers. These points have been reclassified to a separate area not to be used in further processing. The number of removed points was 613,371, which represented 9.3% of the total number of points in the building class.

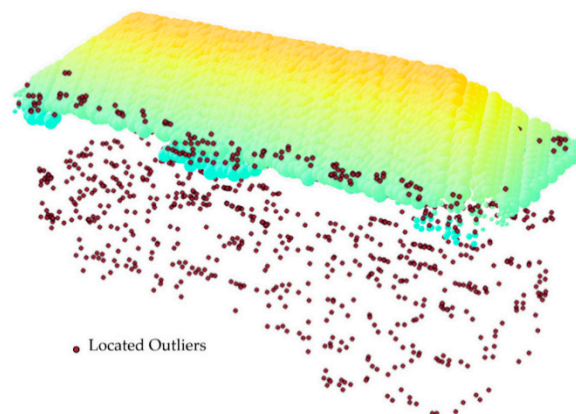


Figure 12. Display of points belonging to the “building” class with the identification of outlier roof points.

3.3. Detection, Segmentation, and Extraction of Roof Objects

To identify the roof polygons used in a class (06 building) with a reduced number of 5,696,591 points, six different types of roofs shown in Figure 13 were selected to illustrate the processing procedure. Object (a) is a fuel station where the roof is a relatively flat surface with a slight slope. Building (b) is an apartment building with a flat roof; in the middle of the roof of the building, there is an elevator engine room. Object (c) is a shopping center with a flat roof with a slight slope. The slope of the roof surfaces mentioned so far is $\alpha \leq 10^\circ$. The following group of buildings represent family houses with a specific type of roof with a slope of $10^\circ < \alpha < 45^\circ$.

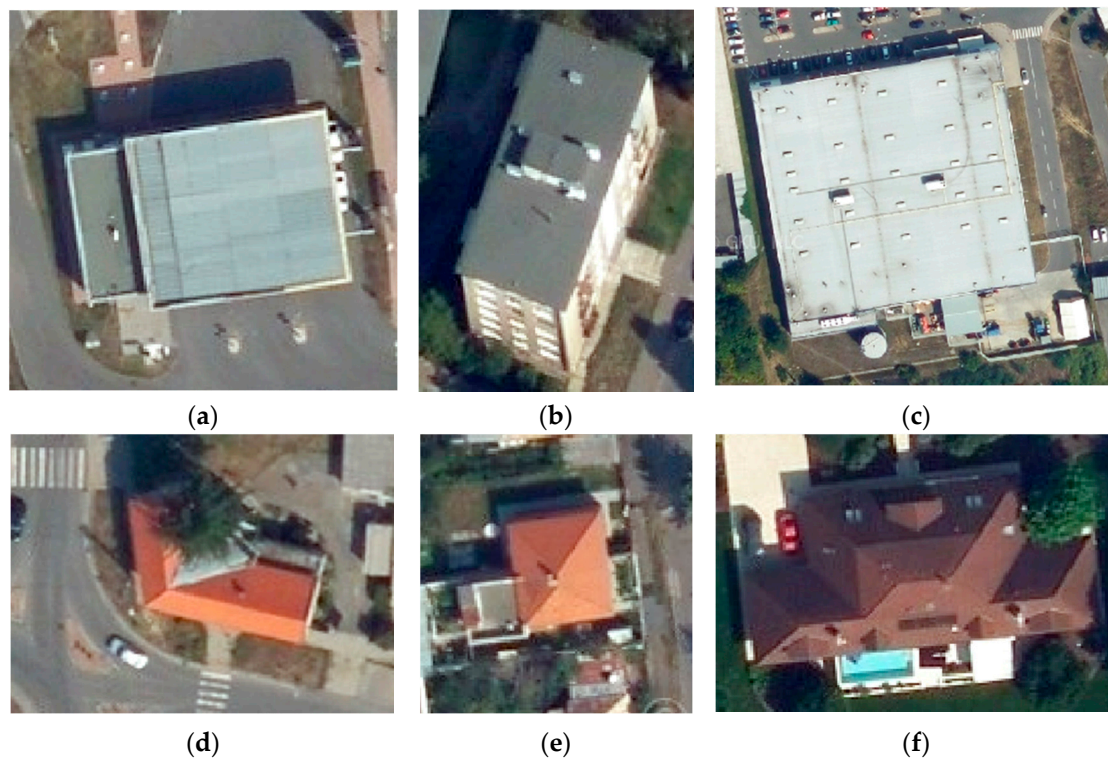


Figure 13. Selected types of roofs (objects) based on orthophoto maps: (a) fuel filling station; (b) an apartment building; (c) shopping center (reduction to 33.3%); (d–f) a family house with a specific type of roof.

The first processing step was to identify the edges of the roof areas. A raster was created from the LiDAR data (Class 6—buildings) to determine the course of the roof edges. Different raster cell sizes (0.3, 0.5, and 1.0 m) were selected to test the detail of the generated raster output. A comparison of the created raster with different cell sizes is shown in Figure 14. During the creation of the polygons, the preservation of the orthogonal shape of the object was taken into account.

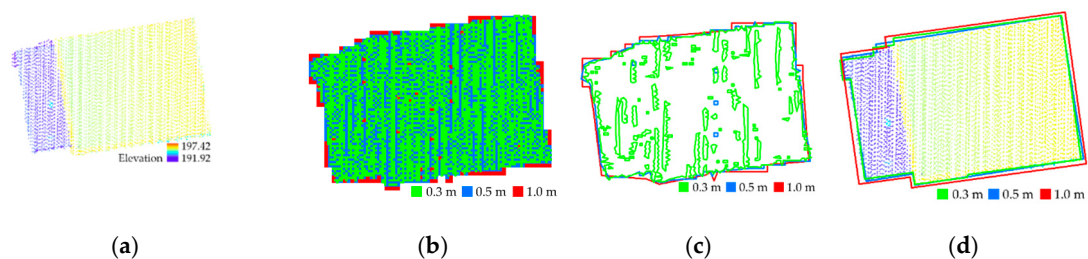


Figure 14. A comparison of roof boundary detection according to raster cell size (m): (a) LiDAR point cloud; (b) creating a raster; (c) aggregation; (d) regularization displayed based on the LiDAR point cloud.

By previous raster cell size analysis, a raster with a cell size of 0.3 m used for the object extraction process. The purified file data were then further processed. The objects (Figure 15) were in terms of their processing divided into two groups: (a–c) represent flat roofs, (d–f) represent sloping roofs. The extracted objects are segmented in the next processing part. The segmentation process of roof surfaces was realized with the procedures in the ArcGIS Pro environment, according to [43]: Simplify Building and Regularize Building (Figure 15(3): (a)–(f)). The same procedure of segmentation could not apply to all types of roofs. When segmenting flat roofs, it was not necessary to detect the roof ridge (Figure 15(1): (a)–(c)). The main idea of pitched roof segmentation realized the concept of modeling the roof ridge. This process depends on the results of the segmentation. Pitched roofs require the use of the Flow direction method, which ensured the detection/identification of the ridge-ridges, hips, and valleys of the roof from the grid (Figure 15(1): (d)–(f)). The subsequent conversion of the raster to the vector format made it possible to obtain segments defining the modeled roof area's actual shape. This step, when applied to all types of roofs, provided a realistic model of the roof (Figure 15(2): (a)–(f)). Subsequently, aggregation and regularization tools are used in the process of roof generalization. Edges transformed into segments of irregular closed polygons required their aggregation. The resulting generalization of the roof area while maintaining the condition of the minimum area of the roof segment, the squareness of the edges, and a closed simple polygon without gaps was provided by two generalization tools—i.e., Simplify Building and Regularize Building (Figure 15(3): (a)–(f)).

The problem of using the LiDAR data source for the identification of roof areas is also the point cloud's density. The LLS process has a problem capturing the boundary roof surfaces because scanning is one of the non-selective data collection methods. In the case of objects located on the roof (chimneys, air conditioning, drainage equipment-gutters, etc.), the problem is their small size compared to the average distance of points. At low point densities, these objects do not detect or are detectable with an insufficient number of points. In the study, we used the LiDAR data source with an average density of 19 points per m^{-2} (with an average distance between adjacent points of 0.23 m). We recommend that if it is necessary to capture more precise details of the roof in the identification, it is more appropriate to use a higher density of points. The related problem is solved [57], which points out the issues related to small parts of the roofs, which may not be sufficiently captured, and thus we recommend choosing a higher density of cloud points.

Outliers identified by an automatic process that did not ensure their complete detection. This process was supplemented by the manual checking of objects. In the case of an automated process, the incorrect identification of points may occur, such as the chimney. This processing part is significant even if we want to create a detailed model of the roof.

The raster cell size density generated from the LiDAR data represents a limiting element of further spatial analyses with a view of the interpolation method used [58,59]. The size of the raster cell should depend on the average density of points, respectively, of the average distance of points. From the studied scientific works [60,61] devoted to the issue of modeling the roof ridge, modeling the direction of surface water runoff (flow direction) is proving to be a suitable method—this method is used regardless of the number of objects.

The process of segmentation itself required an individual approach due to the diversity of the representation of roof types in a given location. Based on our findings, within the specifics of our case study, six basic roofs were selected. It was found that the information on the kind of roof and the number of segments were needed by processing. A set of these characteristics would greatly facilitate the process of selecting these objects for automatic processing. A recommendation for the future is to add necessary data on the type of roof and its segments to datasets within the state information systems (ZBGIS, Real Estate Cadastre). The availability of this group of data would significantly simplify the process of automatic roof segmentation. Spatial analysis, according to [57] parameters such as the geometry of the territory, morphometric properties, and spatio-temporal arrangement, was performed on the whole study area. The result of this part of the study is that roof areas are colored according to selected geometric and topological parameters [62].

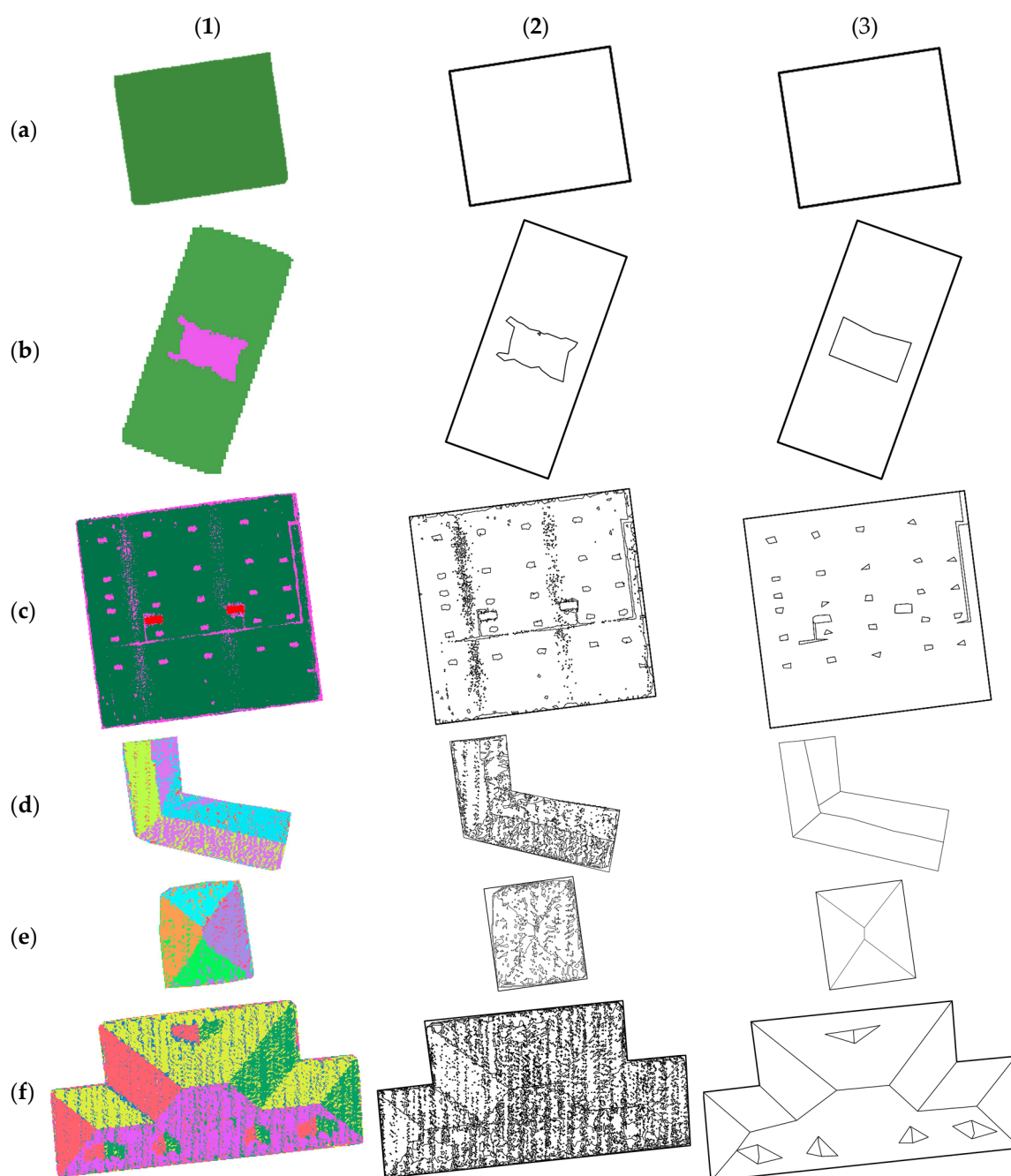


Figure 15. Graphical visualization of the modeling process of selected types of roof surfaces: (1) Detection result; (2) segmentation result; (3) generalization result.

The analysis of the slope ratios of all roof areas (824 roofs) established by the ArcGIS Pro environment used a geoprocessing tool in the 3D Analyst Tools category with a set classification of up to seven classes (Table 5). In our study, we wanted to the basis of a mainly from two groups of roof surfaces (sloping roofs with a roof pitch of $10^\circ < \alpha < 45^\circ$ and flat roofs with an angle of $\alpha \leq 10^\circ$, with a recommended minimum slope of 2%). From the results, according to [63], we applied a seven-level classification. The reason was to capture all changes in the slope conditions of the site.

The azimuth orientation of roofs classified into eight classes according to the value of the azimuth and the corresponding colored roof area (roof areas colored) (Table 6, 4th column). Subsequently, these results were reclassified only into two classes (Table 6, 5th column) according to the suitability of their use for the needs of installation of systems using the amount of incident solar radiation.

Table 5. Reclassification of slope analysis.

Slope Value [°]	Classified Value	Roof Categories	Colored Scale
0–10	1	flat	
10–20	2	sloping	
20–30	3	sloping	
30–40	4	sloping	
40–50	5	sloping	
50–60	6	roof objects	
60–90	7	roof objects	

Table 6. Reclassification of aspect (azimuth) analysis.

Azimuth Value [°]	Azimuth Orientation	Classified Value	Colored Scale	Recolored Scale
0–22.5	North	1		
22.5–67.5	North-east	2		
67.5–112.5	East	3		
112.5–157.5	South-east	4		
157.5–202.5	South	5		
202.5–247.5	South-west	6		
247.5–292.5	West	7		
292.5–337.5	North-west	8		
337.5–360...	North	9		

In a selected part of the study area, we presented the spatial analysis results with a view of the clarity and legibility of the graphic form of the visualization. The result was a representation of the positional and height ratios (Figure 16a), slope ratios (Figure 16b), the azimuth orientation of roof surfaces (Figure 16c), as well as the selection of suitable roof surfaces in terms of further possible usability (installation of systems using the amount of incident solar radiation) (Figure 16d).

On mid-rise buildings is a visible difference in the achieved processing outputs from the level of presence of points of the outlier's group in the LiDAR file. Their presence in the results can cause incorrect classification of the roof's boundary during the analyses. For example, in slope analysis, the roof's boundary presented with red color (Figure 17a), which according to Table 5, represents a very steep slope roof (up to 90°), presenting the facades of buildings. Additionally, in the analysis of height conditions, the presence of color from the non-adjacent height interval (yellow corresponding to the blue edge) is visible on the boundary of the roofs (Figure 17b). Removing outliers points during processing is reflected in the visualization of the slope of the roof surfaces in the form of a uniform color of the roof surface (e.g., without red boundary or colors from lower height intervals).

From the results of the slope analysis (Figure 16b), is possible to identify flat roofs that show the potential for green roofs (dark green color). The results of the azimuth-orientation analysis (Figure 16c,d) provide the potential for the installation of solar systems. These buildings need supplementing by the technical parameters required for the installation of these systems.

The results of this case study form the basis for the identification of roof areas and the creation of 3D models of buildings/cities for a larger territory at the level of details 2 (LOD 2). The proposed method represents an easy and fast solution for the approximate determination of the usability of roof areas. The proposed method shows good results in the case of simple and regular types of roofs. For a more complex roof structure, an individual approach is suitable for more accurate capture of the

geometry of the building. Three-dimensional urban models are used to create urban ecosystems for sustainable urban planning [64].

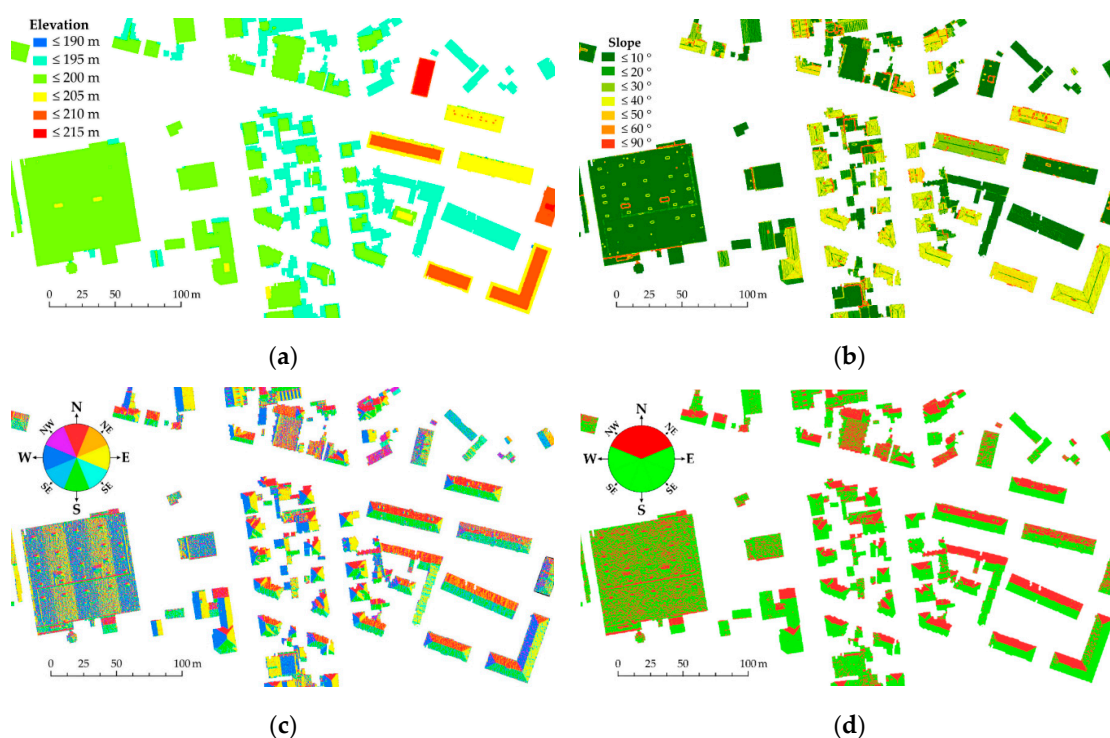


Figure 16. Analysis of LiDAR data: (a) LiDAR point cloud by height, (b) slope, (c) aspect. (d) Classification of LiDAR data according to favorable (green) or unfavorable (red) Azimuth orientation.

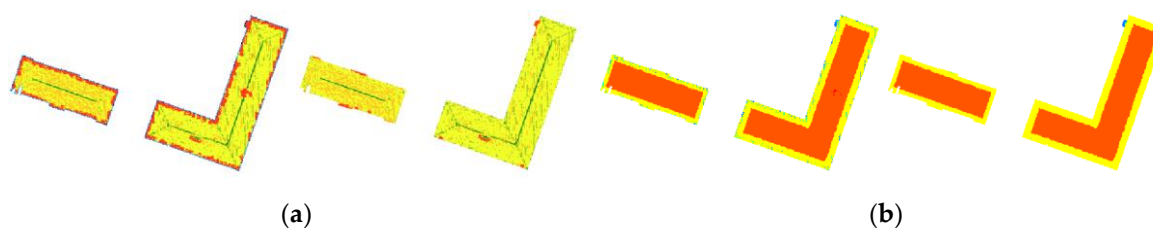


Figure 17. Comparison of LiDAR point cloud processing before and after removing the outlier points on the selected two apartment buildings: (a) slope analysis; (b) elevation analysis.

With climate change (warming), cities face an increased frequency and extent of extreme natural hazards and weather events, such as rising temperatures in growing cities (the formation of heat islands), severe storms, droughts, and floods from local storms. Without the possibility of knowing the space in which we live, it is impossible to face these challenges. As other studies [65] show, building roofs offer the potential to address the synergistic functioning of urban ecosystems. The identification of roof surfaces from LiDAR data in combination with the results of other collection methods opens up space for the creation of object geometry. The acquired properties of residential buildings (geometric and morphometric properties, the roof height of buildings) allow various types of spatial analyses. Knowledge of geometric and topological conditions of residential buildings forms the basis of the calculation of incident solar radiation on roof areas.

Within the European Union, the share of fossil fuel power plants is declining overall, and more is being invested in renewable energy sources also by Directive (EU) 2018/2001 and the Council of 11 December 2018 on the promotion of the use of energy from renewable sources. In the conditions of the Slovak Republic, the subsidy support according to Act no. 309/2009 Coll. on the Support of Renewable Energy Sources and Highly Efficient Combined Production ([www.slov-lex.sk/pravne-](http://www.slov-lex.sk/pravne)

[predpisy/SK/ZZ/2009/309/](#)) enables the installation of equipment with an output of up to 100 kW placed on the roof structure or perimeter cladding of one building connected to the ground by a solid foundation registered in the Real Estate Cadastre. Additionally, for this reason it is necessary to know the theoretical potential of roof areas in the city within the construction of green cities in Slovakia.

The connection of results from our study with the database of descriptive properties or building information model (BIM) opens up space for the creation of a comprehensive database usable in the field of building design and architecture within the framework of sustainable urban planning strategy.

4. Conclusions

This study focused on the topic of identifying the roof areas of residential buildings to operatively determine the essential characteristics of these buildings in the construction of smart cities. The framework of this study proposed an emphasis on maintaining the regularity of the roof boundary, regarding the study aim.

We proposed a solution for extracting the contour and segments of the individual parts of roofs from the LiDAR data source. In solving this, we have used GIS tools complying the following sequence of steps. The first step was to assess the quality of the input data available from official public sources, guaranteeing the origin and quality of the spatial data. LiDAR data was the result of the first step, which ensured compliance with quality requirements. In the next level, these files provided the basis for the creation of a raster input, which served to identify the boundary of the roof surface of irregular shape. Methods of generalization created the contours of the roof surface boundary in a simplified regular form. From the total number of buildings in the examined area (824 roofs), six types of roofs were selected according to the chosen selection criteria. The segmentation process generated segments inside the roof boundary above the level of the selected group of objects.

The visualization of the analyses of selected geometric and topological parameters of roof surfaces was the last level of the study. The obtained results and the proposed solution represent a suitable basis for possible application in the field of potential determination for solar systems or green roofs in the field of building smart cities. As for future research, this study represents the basis for further research in the field of determining the solar potential of roof areas in the conditions of the Slovak Republic. Part of further research also includes the issue of green roofs and their impact on reducing the temperature in residential areas.

Author Contributions: Conceptualization, M.B.G., S.L., and Z.K.; methodology M.B.G., Z.K., and S.L.; software, Z.K.; validation, S.K., S.L., and M.B.G.; formal analysis, S.K.; investigation, Z.K.; resources M.B.G., and Z.K.; data curation, S.L., and S.K.; writing—original draft preparation, S.L.; writing—review and editing, S.K.; visualization, M.B.G., Z.K., S.L., and S.K.; supervision, H.P. All authors have read and agreed to the published version of the manuscript.

Funding: This research was funded by the Scientific grant agency of Ministry of Education, science, research, and sport of the Slovak Republic, grant number 1/0754/18 and 1/0515/18.

Conflicts of Interest: The authors declare no conflict of interest. The funders had no role in the design of the study; in the collection, analysis, or interpretation of data; in the writing of the manuscript; or in the decision to publish the results.

References

1. Directorate General for Regional Policy, European Commission. *Cities of Tomorrow—Challenges, Visions, Ways Forward*; European Union: Luxembourg, 2011. [[CrossRef](#)]
2. Al-Bilbisi, H. Spatial Monitoring of Urban Expansion Using Satellite Remote Sensing Images: A Case Study of Amman City, Jordan. *Sustainability* **2019**, *11*, 2260. [[CrossRef](#)]
3. Liu, T.; Yang, X. Monitoring land changes in an urban area using satellite imagery, GIS and landscape metrics. *Appl. Geogr.* **2015**, *56*, 42–54. [[CrossRef](#)]
4. Diaz-Pacheco, J.; Gutiérrez, J. Exploring the limitations of CORINE Land Cover for monitoring urban land-use dynamics in metropolitan areas. *J. Land Use Sci.* **2014**, *9*, 243–259. [[CrossRef](#)]

5. Ovejero-Campos, A.; Fernández, E.; Ramos, L.; Bento, R.; Méndez-Martínez, G. Methodological limitations of CLC to assess land cover changes in coastal environments. *J. Coast. Conserv.* **2019**, *23*, 657–673. [[CrossRef](#)]
6. Becker, T.; Nagel, C.; Kolbe, T.H. Semantic 3D modeling of multi-utility networks in cities for analysis and 3D visualization. In *Progress and New Trends in 3D Geoinformation Sciences. Lecture Notes in Geoinformation and Cartography*; Pouliot, J., Daniel, S., Hubert, F., Zamyadi, A., Eds.; Springer: Berlin/Heidelberg, Germany, 2013.
7. Kutzner, T.; Hijazi, I.; Kolbe, T.H. Semantic Modelling of 3D Multi-Utility Networks for Urban Analyses and Simulations. *Int. J. 3-D Inf. Model.* **2018**, *7*, 1–34. [[CrossRef](#)]
8. Billen, R.; Cutting-Decelle, A.-F.; Marina, O.; de Almeida, J.-P.; Matteo, C.; Falquet, G.; Leduc, T.; Métral, C.; Moreau, G.; Perret, J.; et al. *3D City Models and Urban Information: Current Issues and Perspectives*; Edpsciences: Les Ulis, France, 2014.
9. Biljecki, F.; Stoter, J.; Ledoux, H.; Zlatanova, S.; Çöltekin, A. Applications of 3D city models: State of the art review. *ISPRS Int. J. Geo-Inf.* **2015**, *4*, 2842–2889. [[CrossRef](#)]
10. Brito, M.C.; Redweik, P.; Catita, C.; Freitas, S.; Santos, M. 3D solar potential in the urban environment: A case study in lisbon. *Energies* **2019**, *12*, 3457. [[CrossRef](#)]
11. Machete, R.; Falcão, A.P.; Gomes, M.G.; Moret Rodrigues, A. The use of 3D GIS to analyze the influence of urban context on buildings' solar energy potential. *Energy Build.* **2018**, *177*, 290–302. [[CrossRef](#)]
12. Santos, T.; Tenedório, J.A.; Gonçalves, J.A. Quantifying the city's green area potential gain using remote sensing data. *Sustainability* **2016**, *8*, 1247. [[CrossRef](#)]
13. Grunwald, L.; Heusinger, J.; Weber, S. A GIS-based mapping methodology of urban green roof ecosystem services applied to a Central European city. *Urban For. Urban Green.* **2017**, *22*, 54–63. [[CrossRef](#)]
14. Riffat, S.; Powell, R.; Aydin, D. Future cities and environmental sustainability. *Futur. Cities Environ.* **2016**, *2*, 1. [[CrossRef](#)]
15. Haarstad, H.; Wathne, M.W. Are smart city projects catalyzing urban energy sustainability? *Energy Policy* **2019**, *129*, 918–925. [[CrossRef](#)]
16. Dornaika, F.; Moujahid, A.; El Merabet, Y.; Ruichek, Y. Building detection from orthophotos using a machine learning approach: An empirical study on image segmentation and descriptors. *Expert Syst. Appl.* **2016**, *58*, 130–142. [[CrossRef](#)]
17. Malof, J.M.; Bradbury, K.; Collins, L.M.; Newell, R.G. Automatic detection of solar photovoltaic arrays in high resolution aerial imagery. *Appl. Energy* **2016**, *183*, 229–240. [[CrossRef](#)]
18. Gamba, P.; Houshmand, B.; Sacconi, M. Detection and extraction of buildings from interferometric SAR data. *IEEE Trans. Geosci. Remote Sens.* **2000**, *38*, 611–617. [[CrossRef](#)]
19. Verma, V.; Kumar, R.; Hsu, S. 3D building detection and modeling from aerial LIDAR data. In Proceedings of the IEEE Computer Society Conference on Computer Vision and Pattern Recognition (CVPR'06), New York, NY, USA, 17–22 June 2006.
20. Ramiya, A.M.; Nidamanuri, R.R.; Krishnan, R. Segmentation based building detection approach from LiDAR point cloud. *Egypt. J. Remote Sens. Space Sci.* **2017**, *20*, 71–77. [[CrossRef](#)]
21. Awrangjeb, M.; Ravanbakhsh, M.; Fraser, C.S. Automatic detection of residential buildings using LIDAR data and multispectral imagery. *ISPRS J. Photogramm. Remote Sens.* **2010**, *65*, 457–467. [[CrossRef](#)]
22. Demir, N.; Poli, D.; Baltsavias, E. Extraction of Buildings using Images & Lidar Data and a Combination of Various Methods. *Int. Arch. Photogramm. Remote Sens. Spat. Inf. Sci.* **2009**, *XXXVIII*, 71–76. [[CrossRef](#)]
23. Vu, T.T.; Yamazaki, F.; Matsuoka, M. Multi-scale solution for building extraction from LiDAR and image data. *Int. J. Appl. Earth Obs. Geoinf.* **2009**, *11*, 281–289. [[CrossRef](#)]
24. Peng, J.; Zhang, D.; Liu, Y. An improved snake model for building detection from urban aerial images. *Pattern Recognit. Lett.* **2005**, *26*, 587–595. [[CrossRef](#)]
25. Kabolizade, M.; Ebadi, H.; Ahmadi, S. An improved snake model for automatic extraction of buildings from urban aerial images and LiDAR data. *Comput. Environ. Urban Syst.* **2010**, *34*, 435–441. [[CrossRef](#)]
26. Zhao, C.G.; Zhuang, T.G. A hybrid boundary detection algorithm based on watershed and snake. *Pattern Recognit. Lett.* **2005**, *26*, 1256–1265. [[CrossRef](#)]
27. Lou, S.; Pagani, L.; Zeng, W.; Jiang, X.; Scott, P.J. Watershed segmentation of topographical features on freeform surfaces and its application to additively manufactured surfaces. *Precis. Eng.* **2020**, *63*, 177–186. [[CrossRef](#)]
28. Zhang, H.; Tang, Z.; Xie, Y.; Gao, X.; Chen, Q. A watershed segmentation algorithm based on an optimal marker for bubble size measurement. *Measurement* **2019**, *138*, 182–193. [[CrossRef](#)]

29. Osma-Ruiz, V.; Godino-Llorente, J.I.; Sáenz-Lechón, N.; Gómez-Vilda, P. An improved watershed algorithm based on efficient computation of shortest paths. *Pattern Recognit.* **2007**, *40*, 1078–1090. [[CrossRef](#)]
30. Lux, F.; Matula, P. DIC image segmentation of dense cell populations by combining deep learning and watershed. In Proceedings of the 2019 IEEE 16th International Symposium on Biomedical Imaging (ISBI 2019), Venice, Italy, 8–11 April 2019.
31. Zhang, J.X.; Lin, X.G. Object-based classification of urban airborne lidar point clouds with multiple echoes using SVM. *ISPRS Ann. Photogramm. Remote Sens. Spatial Inf. Sci.* **2012**, *I-3*, 135–140. [[CrossRef](#)]
32. Kim, A.M.; Olsen, R.C.; Kruse, F.A. Methods for LiDAR point cloud classification using local neighborhood statistics. In Proceedings of the Laser Radar Technology and Applications XVIII, Baltimore, MD, USA, 29 April–3 May 2013.
33. Zhao, Z.; Cheng, Y.; Shi, X.; Qin, X. Classification method of LiDAR point cloud based on threedimensional convolutional neural network. *J. Phys. Conf. Ser.* **2019**, *1168*, 062013. [[CrossRef](#)]
34. Wang, A.; Wang, M.; Wu, H.; Jiang, K.; Iwahori, Y. A novel LiDAR data classification algorithm combined capsnet with resnet. *Sensors* **2020**, *20*, 1151. [[CrossRef](#)]
35. Meng, X.; Currit, N.; Zhao, K. Ground filtering algorithms for airborne LiDAR data: A review of critical issues. *Remote Sens.* **2010**, *2*, 833–860. [[CrossRef](#)]
36. Huang, R.; Yang, B.; Liang, F.; Dai, W.; Li, J.; Tian, M.; Xu, W. A top-down strategy for buildings extraction from complex urban scenes using airborne LiDAR point clouds. *Infrared Phys. Technol.* **2018**, *92*, 203–218. [[CrossRef](#)]
37. Kim, C.; Habib, A. Object-based integration of photogrammetric and LiDAR data for automated generation of complex polyhedral building models. *Sensors* **2009**, *9*, 5679–5701. [[CrossRef](#)] [[PubMed](#)]
38. Awrangjeb, M. Using point cloud data to identify, trace, and regularize the outlines of buildings. *Int. J. Remote Sens.* **2016**, *37*, 551–579. [[CrossRef](#)]
39. Maltezos, E.; Ioannidis, C. Automatic extraction of building roof planes from airborne lidar data applying an extended 3d randomized Hough transform. *ISPRS Ann. Photogramm. Remote Sens. Spat. Inf. Sci.* **2016**, *3*, 209–216. [[CrossRef](#)]
40. Höfle, B.; Mücke, W.; Dutter, M.; Rutzinger, M.; Dorninger, P. Detection of Building Regions Using Airborne Lidar—A New Combination of Raster and Point Cloud Based GIS Methods. In Proceedings of the GI_Forum 2009: International Conference on Applied Geoinformatics, Salzburg, Austria, 7 July 2009; pp. 66–75.
41. Zhang, C.; He, Y.; Fraser, C.S. Spectral Clustering of Straight-Line Segments for Roof Plane Extraction from Airborne LiDAR Point Clouds. *IEEE Geosci. Remote Sens. Lett.* **2018**, *15*, 267–271. [[CrossRef](#)]
42. Dos Santos, R.C.; Galo, M.; Carrilho, A.C. Extraction of Building Roof Boundaries from LiDAR Data Using an Adaptive Alpha-Shape Algorithm. *IEEE Geosci. Remote Sens. Lett.* **2019**, *16*, 1289–1293. [[CrossRef](#)]
43. El Merabet, Y.; Meurie, C.; Ruichek, Y.; Sbihi, A.; Touahni, R. Building roof segmentation from aerial images using a line-and region-based watershed segmentation technique. *Sensors* **2015**, *15*, 3172–3203. [[CrossRef](#)] [[PubMed](#)]
44. Slovenský Hydrometeorologický Ústav. *Climate Atlas of Slovakia*; Slovenský Hydrometeorologický Ústav: Bratislava, Slovakia, 2015; ISBN 978-80-88907-91-6.
45. Redweik, P.; Catita, C.; Brito, M. Solar energy potential on roofs and facades in an urban landscape. *Sol. Energy* **2013**, *97*, 332–341. [[CrossRef](#)]
46. Le, T.B.; Kholdi, D.; Xie, H.; Dong, B.; Vega, R.E. LiDAR-based solar mapping for distributed solar plant design and grid integration in San Antonio, Texas. *Remote Sens.* **2016**, *8*, 247. [[CrossRef](#)]
47. Yu, B.; Liu, H.; Wu, J.; Hu, Y.; Zhang, L. Automated derivation of urban building density information using airborne LiDAR data and object-based method. *Landsc. Urban Plan.* **2010**, *98*, 210–219. [[CrossRef](#)]
48. Triglav Čekada, M.; Crosilla, F.; Kosmatin Fras, M. Theoretical lidar point density for topographic mapping in the largest scales. *Geod. Vestn.* **2010**, *54*. [[CrossRef](#)]
49. Droščák, B. Súradnicový Systém Jednotnej Trigonometrickej Siete Katastrálnej a jeho vzťah k Európskemu Terestrickému Referenčnému Systému 1989. Available online: https://www.geoportal.sk/files/gz/etrs89_s-jtsk_tech_sprava_2014_ver3_0.pdf (accessed on 5 March 2020).
50. Demir, N. Automated Detection of 3D Roof Planes from Lidar Data. *J. Indian Soc. Remote Sens.* **2018**, *46*, 1265–1272. [[CrossRef](#)]

51. Palmer, D.; Koumpli, E.; Cole, I.; Gottschalg, R.; Betts, T. A GIS-based method for identification of wide area rooftop suitability for minimum size PV systems using LiDAR data and photogrammetry. *Energies* **2018**, *11*, 3506. [[CrossRef](#)]
52. Margolis, R.; Gagnon, P.; Melius, J.; Phillips, C.; Elmore, R. Using GIS-based methods and lidar data to estimate rooftop solar technical potential in US cities. *Environ. Res. Lett.* **2017**, *12*, 074013. [[CrossRef](#)]
53. Widyaningrum, E.; Gorte, B.; Lindenbergh, R. Automatic building outline extraction from ALS point clouds by ordered points aided hough transform. *Remote Sens.* **2019**, *11*, 1727. [[CrossRef](#)]
54. O'Callaghan, J.F.; Mark, D.M. The extraction of drainage networks from digital elevation data. *Comput. Vision Graph. Image Process.* **1984**, *28*, 323–344. [[CrossRef](#)]
55. Qin, C.; Zhu, A.X.; Pei, T.; Li, B.; Zhou, C.; Yang, L. An adaptive approach to selecting a flow-partition exponent for a multiple-flow-direction algorithm. *Int. J. Geogr. Inf. Sci.* **2007**, *21*, 443–458. [[CrossRef](#)]
56. Tarboton, D.G. A new method for the determination of flow directions and upslope areas in grid digital elevation models. *Water Resour. Res.* **1997**, *33*, 309–319. [[CrossRef](#)]
57. Lukač, N.; Seme, S.; Žlaus, D.; Štumberger, G.; Žalik, B. Buildings roofs photovoltaic potential assessment based on LiDAR (Light Detection And Ranging) data. *Energy* **2014**, *66*, 598–609. [[CrossRef](#)]
58. Polat, N.; Uysal, M.; Toprak, A.S. An investigation of DEM generation process based on LiDAR data filtering, decimation, and interpolation methods for an urban area. *Meas. J. Int. Meas. Confed.* **2015**, *75*, 50–56. [[CrossRef](#)]
59. Lloyd, C.D.; Atkinson, P.M. Deriving DSMs from LiDAR data with kriging. *Int. J. Remote Sens.* **2002**, *23*, 2519–2524. [[CrossRef](#)]
60. Shan, W.; Tamura, Y.; Yang, Q.; Li, B. Effects of curved slopes, high ridges and double eaves on wind pressures on traditional Chinese hip roofs. *J. Wind Eng. Ind. Aerodyn.* **2018**, *183*, 68–87. [[CrossRef](#)]
61. Lingfors, D.; Bright, J.M.; Engerer, N.A.; Ahlberg, J.; Killinger, S.; Widén, J. Comparing the capability of low- and high-resolution LiDAR data with application to solar resource assessment, roof type classification and shading analysis. *Appl. Energy* **2017**, *205*, 1216–1230. [[CrossRef](#)]
62. Martín-Jiménez, J.; Del Pozo, S.; Sánchez-Aparicio, M.; Lagüela, S. Multi-scale roof characterization from LiDAR data and aerial orthoimagery: Automatic computation of building photovoltaic capacity. *Autom. Constr.* **2020**, *109*, 102965. [[CrossRef](#)]
63. Matei, B.C.; Sawhney, H.S.; Samarasekera, S.; Kim, J.; Kumar, R. Building segmentation for densely built urban regions using aerial LIDAR data. In Proceedings of the 2008 IEEE Conference on Computer Vision and Pattern Recognition, Anchorage, AK, USA, 23–28 June 2008.
64. Grêt-Regamey, A.; Celio, E.; Klein, T.M.; Wissen Hayek, U. Understanding ecosystem services trade-offs with interactive procedural modeling for sustainable urban planning. *Landsc. Urban Plan.* **2013**, *109*, 107–116. [[CrossRef](#)]
65. Adeleke, A.K.; Smit, J.L. Building roof extraction as data for suitability analysis. *Appl. Geomatics* **2020**. [[CrossRef](#)]

